X-ray Spectral Analysis of a Serendipitously Observed Active Galactic Nucleus

FILIP AF MALMBORG

TEODOR ELMFELDT
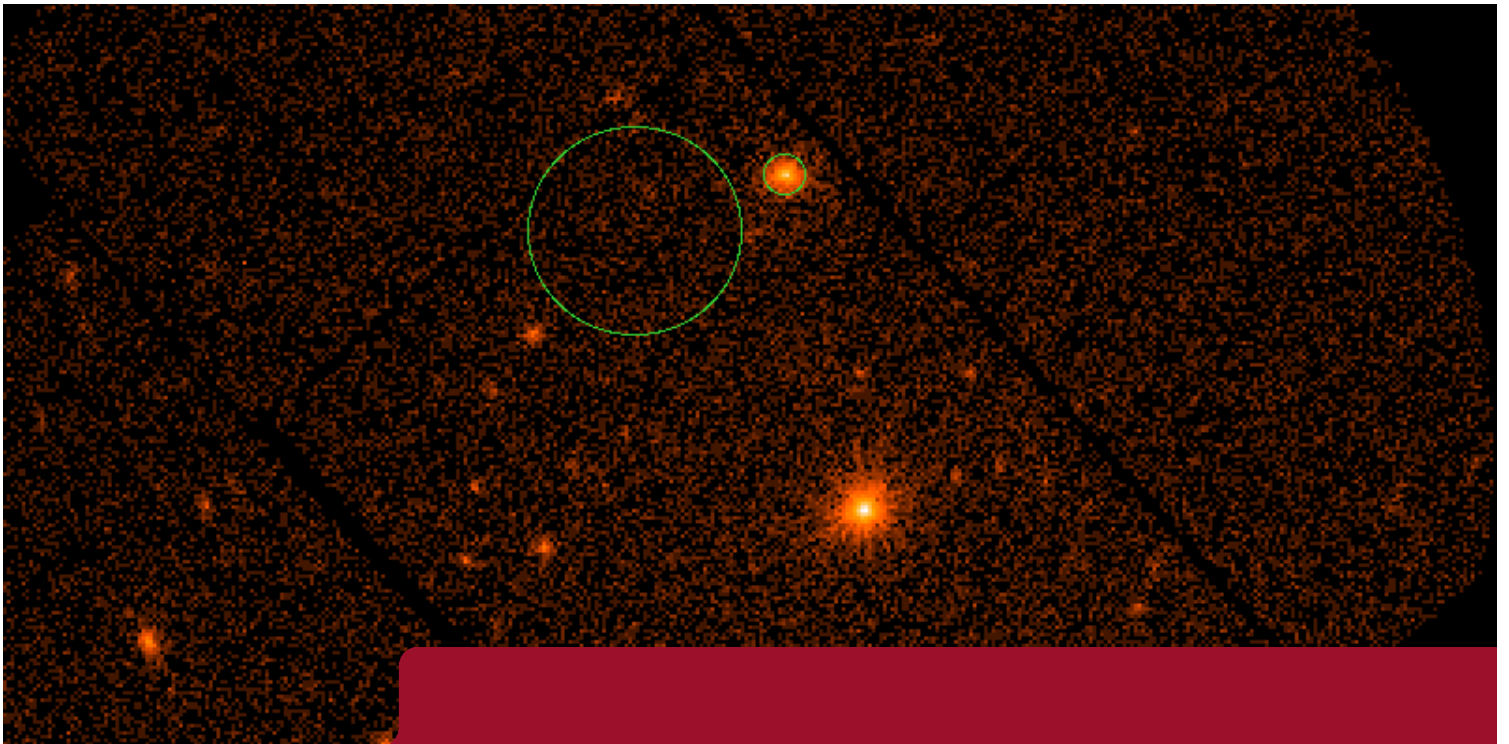
Physics

X-ray Spectral Analysis of a Serendipitously Observed Active Galactic Nucleus

Filip af Malmborg
filipam@kth.se
Teodor Elmfeldt
teodorel@kth.se
SA114X Degree Project in Engineering Physics, First Level
Department of Physics
KTH Royal Institute of Technology
Supervisor: Dennis Alp

June 1, 2020

Abstract

An active galactic nucleus (AGN) is a region in the center of a galaxy with a supermassive black hole continuosly accreting material. This accretion gives rise to large amounts of radiation across the whole electromagnetic spectrum, and largely affects the regions around the AGN and the evolution of the whole galaxy. Using X-ray spectral analysis, a study is performed of a supposed AGN at position J130028.5+283010.1 (celestial coordinates) that was captured as a secondary object during observations of a galaxy cluster in front of *X Comae*. Six observations by *XMM-Newton* during the years 2004–2006 are used, extracted using the XMM-SAS tools and analysed using XSPEC. The analysis shows that this object most probably is an AGN, and the spectrum varies significantly between observations. Furthermore, the later observations show some difficult-to-model features, possibly hinting at the presence of emission reflected in the accretion disk around the supermassive black hole in the center of the AGN. This thesis presents a summary of the spectral properties of the AGN and its evolution over time.

Sammanfattning

En aktiv galaxkärna (AGN) är en region i mitten av en galax med ett supermassivt svart hål som kontinuerligt drar till sig material från omgivningen. Denna ackretion skapar stora mängder strålning över hela det elektromagnetiska spektrumet, och påverkar både regionerna runt AGN:en och hela galaxens utveckling. Med hjälp av röntgenspektralanalys studeras i denna rapport ett objekt, J130028.5+283010.1, som antas vara en AGN. Objektet fångades på bild av röntgenteleskopet *XMM-Newton* sex gånger mellan 2004 och 2006, som ett sekundärt objekt när bilder togs av ett galaxkluster framför galaxen *X Comae*. Dessa sex observationer utgör datan som extraheras med XMM-SAS-verktygen och analyseras med XSPEC. Analysen visar att objektet troligen är en AGN, och spektrat varierar signifikant mellan olika observationer. Vidare finns i de senare observationerna komponenter i spektrumet som är svåra att modellera, och som möjligen tyder på strålning som reflekteras i ackretionsdisken runt det supermassiva svarta hålet i AGN:ens mitt. I den här rapporten presenteras en sammanfattning av AGN:ens spektrala egenskaper samt dess utveckling över tid.

Contents

Chapter 1

Introduction

In astrophysics, one of the main points of interest for today's research is black holes, due to their nature of putting the laws of physics to the most extreme tests. Black holes are objects of immense density, collapsed into a singular point by extreme gravity. Anything inside the *event horizon*, including light, cannot leave the region because of the heavy curvature of spacetime caused by the high density. *Supermassive black holes* (SMBH) are black holes of millions to 10 billion solar masses, to be compared with smaller (stellar) black holes, which are typically on the order of ten solar masses.

While no radiation leaves the black hole itself, many are surrounded by an *accretion disk* where nearby mass is aggregated and its gravitational energy converted into radiation. A SMBH combined with the accretion disk make up the black hole region of *active galactic nuclei* (AGN). While all galaxies are theorised (and thus far observed) to have supermassive black holes in their centers (Lynden-Bell 1969), the ratio of galaxies with active black hole regions seems to be between 10–30%, depending on the age of the universe in the area observed (Hwang et al. 2012). In an AGN, matter continuously falls into the black hole, losing energy and emitting it as radiation in the process. These active black hole regions are among the most luminous persistent objects in the universe, sending out non-stellar radiation at all wavelengths from radio to gamma rays (Beckmann 2012). The study of these is important because they highlight some of the biggest and most extreme processes known, important for the study of fundamental physics and the universe. There is also a complex but important feedback between AGN and their host galaxies, where the activity of the AGN can affect long-term evolution and star formation in the host galaxies (Fabian 2012).

Historically in astronomy, most observations were in the optical (visible) band, but technological advances during the last 100 years have opened up for observations in other parts of the electromagnetic spectrum. Relevant for this thesis is that black holes consuming matter are strong X-ray sources, making them one of the main subjects of study for X-ray astronomy (Beckmann 2012). In particular, AGN are often studied through X-ray spec-

tral analysis, which can provide views into the central regions of AGN to allow them to be studied.

Of the AGN present in the observable universe, many are unstudied. Surveys of the sky in the X-ray band have been done by the *XMM-Newton, Chandra* and *Swift* satellite telescopes, but much of the data has yet to be analysed. One of the hitherto unstudied objects is an X-ray source at sexagesimal coordinates J130028.53+283010.1 (hereafter J130028) observed by *XMM-Newton* six times in the years 2004–2006. Preliminary analysis suggests that the object is an AGN, and in this thesis we will study the properties of this AGN through analysis of the X-ray spectrum.

1.1   Thesis outline

The thesis is structured as follows. First, the necessary background material will be presented in Chapter 2. This consists of background on AGN and their X-ray emission mechanisms, together with information on the telescopes providing data and the software and methods used. Chapter 3 will follow, detailing the method and tools used to perform the study. Then, in Chapter 4, the results will be presented, which mainly consists of spectral analysis. Different models are tested and characteristics and parameters of the AGN will be determined. In Chapter 5, implications for the physical properties are discussed along with a comparison with similar AGN and existing knowledge of AGN. Lastly, Chapter 6 is a summary of the thesis with conclusions.

Chapter 2

Background Material

2.1 Black holes

2.1.1 General background

A black hole is an object with such immense density that it warps spacetime enough to trap all matter and light. The boundary within which nothing can escape is known as the *event horizon*, because no information about any event inside the event horizon can reach outside of it. This is because close enough to the centre of mass, the gravitational escape velocity is above the speed of light. The radius where the escape velocity is equal to the speed of light is known as the Schwarzschild radius, mathematically

$$R_{\mathrm{S}} = \frac{2GM_{\mathrm{BH}}}{c^2},\tag{2.1}$$

where G is the gravitational constant, M_{BH} is the mass of the black hole and c is the speed of light. Another important radius is the *innermost stable circular orbit* (ISCO), which is the smallest distance from the centre where stable orbits are possible. For a non-spinning massive object, this distance is

$$R_{\mathrm{ISCO}} = \frac{6GM_{\mathrm{BH}}}{c^2} = 3R_{\mathrm{S}}.\tag{2.2}$$

When the black hole is spinning, however, the ISCO changes depending on if the spin is prograde (in the same direction as the spin of the accretion disk) or retrograde (in the opposite direction). The spin of black holes is often measured in terms of the spin parameter a, which is defined as

$$a = \frac{cJ}{GM^2},\tag{2.3}$$

where c is the speed of light, J is the black hole angular momentum, G is the gravitational constant and M is the black hole mass (Reynolds 2019). This has the effect that the structure of spacetime around a spinning black hole depends only on a and M, making the spin parameter very useful for simplifying modelling. The spin parameter can also be shown to have a minimum value of -1 (maximal retrograde spin) and a maximum of 1 (maximal prograde spin), since any values outside this range would produce a naked singularity, which does not agree with our current understanding of physics. For the ISCO, the spin parameter changes its value from $R_{\mathrm{ISCO}} = 3R_{\mathrm{S}}$ at 0 spin to $R_{\mathrm{ISCO}} = 4.5R_{\mathrm{S}}$ at maximum retrograde spin ($a = -1$), to $R_{\mathrm{ISCO}} = R_{\mathrm{S}}$ at maximum prograde spin ($a = 1$). This means that the spin largely affects how close matter can persistently stay to the event horizon, and therefore governs the behaviour of the inbound matter.

2.1.2   Black hole accretion disk

In an AGN the source of emitted power is matter constantly falling into the central SMBH, a process known as accretion. In this process, gravitational potential energy in the accreting matter is converted first into kinetic energy and then further into radiation in a highly efficient process, with a ratio of mass-energy conversion in the order of 10%. This can be compared to the 10^{-8}% efficiency of chemical burning, or the 0.7% efficiency of the sun's hydrogen-to-helium fusion. This efficiency, together with the very high mass of the central black hole and the mass-dependency of the Eddington limit (see Section 2.2.2), is key to the extreme luminosity of AGN, allowing them to be observable over enormous distances.

Due to the conservation of angular momentum, the matter falling into the black hole will form an accretion disk (similar to how solar systems or galaxies end up mostly disk-shaped). The standard disk model is that of a geometrically thin and optically thick disk, meaning a disk which has low thickness in the direction of the rotational axis, while being largely impenetrable to radiation. This model of accretion is also known as the Shakura-Sunyaev model, after the authors which first published the theory (Shakura and Sunyaev 1973). This accretion disk typically has its inner limit at the R_{ISCO}, and its outer limit varies with the activity of the black hole and the amount of accreting matter, among other factors.

2.2   Active galactic nuclei

2.2.1   Historical background and geometry

The signs of AGN were first detected during the first half of the 20th century, but understanding of the phenomenon dates back to the emergence of the field of radio astronomy in the 1950's. The large redshift combined with the high luminosity was consistent with theories of non-stellar objects located at enormous distances. These were later identified as

SMBH in the centres of distant galaxies, and the theory of AGN was widely accepted by the 1970's.

AGN are SMBH located at the centre of galaxies, continuously accreting nearby matter. In this process, vast amounts of radiation are emitted, powered by the gravitational potential energy of the incoming matter, see Section 2.1.2. Apart from the accretion disk and black hole, an AGN is hypothesised to consist of regions of gas molecules known as the Near-Line and Broad-Line Regions (NLR and BLR), as well as a torus of gas and dust in the region furthest from the black hole. Figure 2.1 is a schematic view of an AGN, useful for understanding how the parts are connected and why the viewing angle profoundly affects observations.
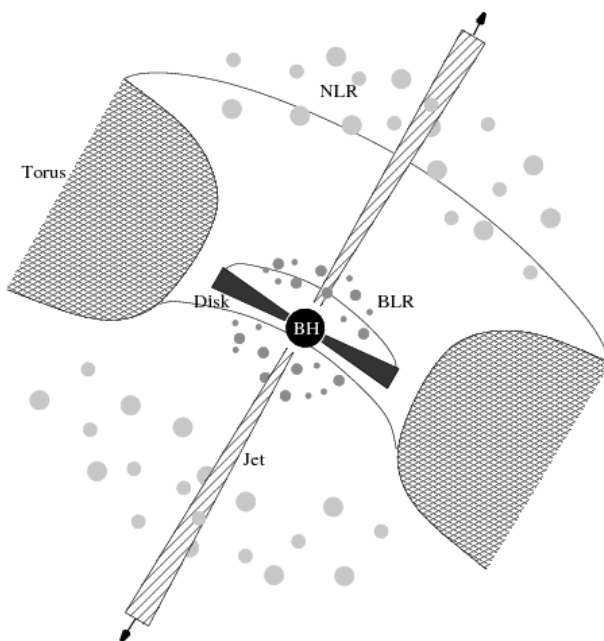
Figure 2.1: Unification scheme for AGN (not to scale), provided by Middelberg and Bach 2008. Note that observations are depending on viewing angle. The schematic is indicative and many exact features are debatable.

2.2.2   Eddington limit

The Eddington limit is an upper limit on the luminosity of any object, in this case an AGN (Beckmann 2012). It is derived from the balance between the outward radiative pressure and the inward gravitational attraction. In order for a SMBH to produce persistent emission, we need the radiative force F_{rad} to be smaller or equal to the gravitational force F_{grav}. If $F_{\mathrm{rad}} > F_{\mathrm{grav}}$, then no new matter would fall into the black hole.

To get a rough approximation of the Eddington luminosity we can assume spherical symmetry, dynamical equilibrium and approximating the accreting gas as fully ionised hydrogen. The outward radiative force is then the result of photons scattering off the ionised electrons and transferring their momentum to them. Further, the radiative force is given by

$$F_{\mathrm{rad}} = \frac{L}{4\pi r^2 E} \cdot \frac{E}{c} \cdot \sigma_T, \tag{2.4}$$

with L being the luminosity of the source (the AGN in this case), r the distance to the source, E the photon energy, c the speed of light and σ_T the Thomson cross section for electron scattering, with a numerical value of $6.65 \cdot 10^{-29}$ m^2. The first factor corresponds to the photon flux, the second to the photon momentum and the third to the interaction probability given by the cross section, giving a physical interpretation of the force as above. Conversely, the gravitational force is given by

$$F_{\mathrm{grav}} = \frac{GM_{\mathrm{BH}}}{r^2}(m_p + m_e), \tag{2.5}$$

where G is the gravitational constant, M_{BH} is the mass of the central black hole and m_p and m_e are the proton and electron masses, respectively.

To get the Eddington luminosity, we set these two forces equal, and with the approximation $m_p + m_e \approx m_p$ we combine Equations 2.4 and 2.5 into

$$L_{\mathrm{Edd}} = \frac{4\pi m_p c G M_{\mathrm{BH}}}{\sigma_T} \approx 1.3 \cdot 10^{38} \frac{M_{\mathrm{BH}}}{M_{\odot}} \text{ erg s}^{-1}. \tag{2.6}$$

Here $M_{\odot}$ is the mass of the sun, since the convention is to express black hole masses in units of solar masses. This equation gives us an upper limit for the luminosity for a black hole of a given mass, and also lets us define the Eddington ratio, which is the ratio between the observed luminosity and the Eddington luminosity of the AGN as $L_{\mathrm{obs}}/L_{\mathrm{Edd}}$. This is one of the key parameters for classifying an AGN, and is correlated with several observable AGN properties. Since the luminosity is closely tied to the accretion of matter in AGN, the Eddington ratio can give information about the processes governing the accretion and the formation of the accretion disk.

2.3   X-ray emission mechanisms of AGN

In the current theory, there are four main contributors to the emission of AGN: the accretion disk, the corona, line emission and a possible jet. None of these mechanisms are fully understood, but they can be used to model AGN to varying degrees of success. Studying

these different components is of particular interest to further our understanding of AGN. This section will go through the emission mechanisms thought to be present in AGN.

2.3.1 Disk emission

The emission from the accretion disk arises from friction between particles in the disk, resulting in heating of the material. From this, the disk emission can be modelled as black-body radiation, meaning that the emitted spectrum is uniquely defined by the temperature. This temperature varies with the disk radius, meaning that the emitted spectrum will be a multicolor black-body spectrum from different parts of the disk.

The model of disk emission predicts the relation between maximal temperature T_{max} of the disk and the mass M_{BH} to be $T_{\mathrm{max}} \propto M_{\mathrm{BH}}^{-1/4}$. This, rather surprisingly, means that higher mass black holes are expected to have a lower T_{max} than lower mass ones. In fact, most AGN are expected to have a disk temperature around 5–20 eV[1] (Bonning et al. 2007), giving a peak of the radiation in the ultraviolet band. Radiation at this wavelength is absorbed to a large degree in the interstellar medium, which makes study of the pure black-body radiation of AGN hard. However, a black-body-like component in the X-ray band is still present in most AGN spectra. This not hypothesised to be the black-body radiation of the accretion disk, but originate from some other emission mechanism. It is usually called the *soft excess* and will be further discussed further in Section 2.3.5.

In conclusion, while the black-body radiation is the primary source (and the only source in absence of a relativistic jet) of the energy emitted from AGN, it is not the primary radiation observed. As we will see in the following sections, the emission is theorised to have many different components, most of which consist of absorption and scattering of the black-body radiation, or reprocessing of the radiation in some other way.

2.3.2 Line absorption and emission

One of the mechanisms affecting the observed spectra of AGN is line emission and absorption of radiation in the gas clouds surrounding the central black holes. Spectral lines are usually in the optical spectra and are caused by the electron configuration of atoms, and since every type of atom has its characteristic lines, it is possible to compare to known spectra to calculate redshift. Line emission is caused by ionisation of atoms: photons of a specific wavelength are emitted when an electron de-excites. Line absorption is caused by photons of a specific wavelength getting captured by an atom that gets excited.

Classically, the lines emitted and absorbed are narrow, and this is the case when the reaction happens far from the black hole. When the lines are generated close to a black hole they become Doppler shifted, broadening them and shifting them to different frequencies.

---

[1]Roughly equal to 60 000–230 000 K

These are so-called broad emission lines and indicate high velocities or deep gravitational potentials causing the Doppler shift. Since the line energies for all elements are known and there are hypotheses for their abundance in AGN, the measured broad lines can be compared to the narrow line profiles. The difference can be used to infer information about the central black hole and the dynamics of its accretion disk, through the theories of special and general relativity.

The characteristic spectral line that we will focus on in this thesis is the Fe K-alpha line, coming from the K-shell of the iron atom. All AGN exhibits the ironline at 6.4 keV, and it is the only clear line that is visible in the X-ray spectra using current instruments. This makes it crucial for comparing different AGN and measuring some of their properties.

2.3.3   Corona

The corona is hypothesised to be the main contributor to the X-ray continuum seen in most AGN. It is located above the accretion disk and consists of extremely hot plasma. Here, emitted black-body photons from the accretion disk undergo inverse Compton scattering which energises them up to X-ray energies. Compton scattering is caused by a charged particle scattering a photon, causing a decrease in energy of the photon. Inverse Compton scattering is the the opposite effect, when a charged particle increases the energy of the photon by transferring part of its energy to the photon. For the X-ray photons in AGN, it is the electrons in the plasma of the corona which provides the energy. These electrons can be assumed to have a number energy distribution $N_e(E)$ according to a power-law distribution

$$N_e(E)\,dE \propto E^{-p}\,dE, \tag{2.7}$$

where $N_e(E)$ is the energy distribution of the electrons in the plasma as a function of electron energy and p is a power-law exponent (Netzer 2013). From this electron power-law distribution, the Comptonized photons get a flux per energy level given by the similar power law expressed as

$$F(E) \propto E^{-(p-1)/2}. \tag{2.8}$$

Here $F(E)$ is the flux as a function of photon energy and p is the power-law exponent. This flux is then related to the photon distribution $N_{ph}(E)$ as $F(E) \propto E \cdot N_{ph}(E)$, which then means that the photon number flux density is described by

$$N_{ph}(E) \propto E^{-(p-3)/2}. \tag{2.9}$$

The exponent of this relation, with the minus sign removed, is often dubbed the photon index and denoted by Γ. The value of Γ varies between AGN, and is one of the key parameters determining the AGN X-ray spectrum. The continuum power-law component thought to originate in the corona is prominent in almost all AGN, and is seen from low X-ray energies

(~ 0.1 keV) up to a sharp drop-off at around 100 keV. This drop-off does not originate in the power-law itself, but rather comes from the fact that at a certain energy the Comptonized photons begin undergoing pair production, producing electron-positron pairs which create radiation without the power-law characteristics. The exact position of the drop-off is dependent on the temperature of the corona, but since the instruments used in this thesis does not cover the usual drop-off range, it will not be studied here.

2.3.4   Jet

Jets are powerful outflows of relativistic particles from AGN, observed in about 10% of AGN and extending up to several Mpc (Willis, Strom, and Wilson 1974). They are thin and well-collimated, meaning that the opening angle is small. The huge scales are possible because of the directional stability of the jets. Observations imply that they always come in pairs, with jets extending in opposite directions. If one of the jets in the pair is directed towards our line of sight, the other jet will be hard to observe.

The emission from the jets is hypothesised to come in two forms: a power-law component produced by inverse Comptonization similar to the corona, but also synchrotron emission produced by the particles in the jet moving at relativistic speeds. This synchrotron emission undergoes heavy relativistic Doppler shifting and spans the whole electromagnetic spectrum. The synchrotron component of the AGN spectrum will not be covered by this thesis, but it is important to note that it is responsible for the radio signal seen in some AGN. This is important, since it means that if a radio signal is present in the AGN, one of the jets is most probably pointed in the direction of Earth. This is indicated by the radio-loudness of the AGN, which is defined as the ratio of radio flux in the 5GHz band (F_5) to the flux in the visible B-band (F_B) (Kellermann et al. 1989). If this ratio is greater than 10 ($F_5/F_B > 10$), the AGN is classified as radio-loud, which provides an easy indication of the presence of jet emission. Lastly, it should also be noted that the formation of the jets is a quite poorly understood process, and there exists no scientific consensus on what governs the presence or absence of jets in AGN.

2.3.5   Soft excess

One of the largest conundrums in the study of AGN is the *soft excess*. This consists of a soft (low-energy) X-ray component below 2 keV in the AGN rest frame which is not captured by the more standard models for AGN X-ray emission, hence the name soft excess (Gierliński and Done 2004). It is present in most AGN with a quite consistent peak energy but with a varying magnitude. This consistent peak of the soft excess over a wide range of AGN mass and luminosity is quite peculiar, since other parts of the spectrum usually varies with mass and luminosity, and is one of the reasons why it is not easily explained by any existing theories. However, it is often fitted quite well by a simple black-body component, but the

temperature of this black-body does not match any theoretically predicted component of the AGN. Typically, the soft excess black-body has a temperature of 100–300 eV (AGN rest frame), far above the disk temperature of ~ 10 eV.

In this thesis, the soft excess will mostly be modelled by a black-body component. This will allow for more accurate fitting of other model components. However, one of the leading theories of the soft excess origin is disk reflection, which will be tested in this thesis.

2.3.6   Disk reflection

The disk reflection model relies on continuum power-law emission, possibly from the AGN corona, illuminating the optically thick accretion disk, together with fluorescent lines from the ionised elements in the disk. When reflected by the disk, this emission is highly smeared out and broadened by effects arising from both special and general relativity (Fabian et al. 2000).

From special relativity, we get both longitudinal and transverse Doppler shifting of the emission. The longitudinal Doppler shift gives rise to what is known as relativistic beaming, resulting in a change of wavelength of the emission from the parts of the disk moving towards or away from the observer. The transverse Doppler effeiments such as the Twin paradox[2]. For the accretion disk of an AGN, this leads to both redshift and blueshift of the emission, again depending on if the emitting parts is moving towards or away from the observer. To these two special relativistic effects is added the gravitational redshift from general relativity, due to the extreme gravitational field in the proximity of the black hole. Since the velocities and gravitational fields governing these effects are different in different parts of the disk, the reflected emission and its components such as emission lines get broadened and shifted, giving rise to a broad continuum-like spectrum. This spectrum can, among other things, explain the presence of the soft excess in most AGN, while the illuminating power-law component can explain the harder X-rays (Crummy et al. 2006). Furthermore, due to the relativistic effects being dependent on the nature of the gravitational field and accretion disk, the shape of the reflected spectrum can be tied to the important spin parameter of the black hole.

The ratio between the direct and reflected parts of the emission can vary, and governs the shape of the spectrum. This reflection fraction is one of the key parameters in determining the shape of the spectrum, together with the photon index Γ of the illuminating power-law component. Two other parameters that affect the spectral shape of the reflected component are the abundance of iron in the disk, which governs the presence of the highly luminous iron K shell lines; as well as the amount to which the disk is ionised, which also affects the presence of line emission. The fine-tuning of these parameters to fit the spectrum from AGN is a matter of some discussion in the field of astrophysics, and particularly the necessity of high iron abundances (up to 10 times the solar amount) is an unsolved problem (García et al.

---

[2]`https://en.wikipedia.org/wiki/Twin_paradox`

2018). Nevertheless, the disk reflection model is widely used to estimate AGN properties such as black hole spin, and will be used in this thesis to achieve good fits to the spectral data and handle the soft excess.

2.4   Interstellar medium absorption

The main object of this thesis is to study the AGN spectrum and it is the findings of the source spectrum analysis which will be reported. However, to get a correct picture of the spectrum the absorption of the interstellar medium (ISM) needs to be considered, both in the Milky Way and possibly in the host galaxy of the AGN.

This absorption is generally inversely proportional to the energy of the X-ray radiation, leading to higher absorption rate of lower energies. The probability of absorption is $e^{-\tau}$, where $\tau \propto E^{-\alpha}$ is the optical depth of the ISM. The parameter α has been experimentally verified to be roughly equal to three. This gives an exponential cutoff of the X-ray radiation at low energies, and is one of the main reasons for AGN's mainly being studied in the X-ray band.

The ISM can be modelled in many different ways, and in this thesis, the Tuebingen-Boulder ISM absorption model will be used. (Wilms, Allen, and McCray 2000). The model allows calculation of the X-ray absorption in the ISM due to presence of many different elements, and allows for varying column densities of different elements. For the purposes of this thesis, a varying hydrogen atom column density is sufficient, with the abundance of other elements kept constant at a value relatively close to solar values, according to the model defaults. This hydrogen atom density of the Milky way has been calculated for the whole sky (Willingale et al. 2013). For the host galaxy, this column density presents a free parameter in the spectrum produced.

2.5   Cosmological redshift

Cosmological redshift is an effect of the expansion of space, causing remote objects to move apart with a relative velocity to Earth approximately proportional to their distance from Earth. The relative velocity causes a Doppler shift which can be estimated by comparing incoming light with expected emission profiles. To calculate this redshift, one needs to take both general and special relativity into consideration. For the special relativistic case, the redshift can be calculated as

$$1 + z = \left(1 + \frac{v}{c} \right) \gamma, \tag{2.10}$$

with z being the redshift, v the velocity relative to Earth, c the speed of light and γ the Lorentz factor. However, at relatively low redshifts, $\gamma \approx 1$, which gives the linear approximation $z \approx \frac{v}{c}$. At higher redshifts, this approximation would not hold and one also needs to consider general relativity to get the recessional velocity, but as can be seen in Figure 2.2, the models generally agree at a redshift lower than 1. (Davis and Lineweaver 2001). With this linear approximation, and using Hubble's law

$$v = H_0 D, \tag{2.11}$$

H_0 being the Hubble constant (in this work set to the standard $H_0 = 70$ km/s/Mpc), it is possible to calculate the distance from Earth D. However, instead of carrying out these calculations, the convention in astrophysics is to use only the z-value for redshift to measure distance, since it captures the information needed about an object and its light spectrum. In this thesis, we will be using the redshift z to properly evaluate the spectrum, but a comment on the distance to the source will also be included.
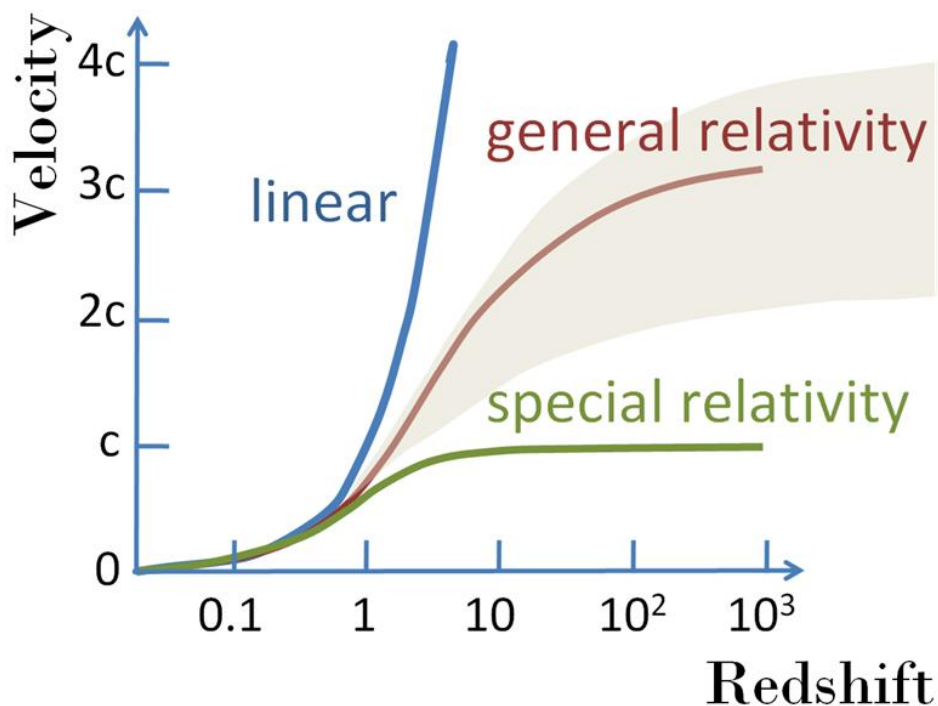
Figure 2.2: Different models for calculating the recessional velocity v from the redshift z. In this thesis, a redshift of $z = 0.64684$ is most often used, and for this redshift it is clear in the figure that the linear model agrees with general relativity. *Image from Brews ohare / CC BY-SA (https://creativecommons.org/licenses/by-sa/3.0)*

2.6   X-ray telescopes

For our study of J130028, we use data from an X-ray telescope. X-rays are defined as photons with energies between 0.1–100 keV, while visible light is about 2–3 eV. Observations in the X-ray band reveal some of the most energetic and extreme phenomena in the universe. X-rays are absorbed by the atmosphere, so X-ray telescopes are placed outside of the atmosphere. Typical exposure times for these X-ray telescopes are 10–100 ks, during which time, energy, and position on the CCD chip are recorded for each photon.

2.6.1   XMM-Newton

The EPIC set of cameras onboard the *XMM-Newton* is the source of observational data in this work and consists of three cameras: Two MOS (Turner, M. J. L. et al. 2001) and one pn (Strüder, L. et al. 2001) camera. In the standard operation mode, used in the observations of this work, it collects observations in the energy range 0.15–15 keV with a field of view of 27.2×26.2 arcmin^2. The angular resolution is 6 arcsec and the spectral resolution is 20–50. Spectral resolution is a measure determined by the ratio of $\lambda/\Delta\lambda$, with $\Delta\lambda$ being the smallest detectable difference around the wavelength λ.

2.6.2   Charge Coupled Device (CCD)

A CCD image sensor is a device that measures incoming photons by detecting electrons that become free when the photon hits them. By measuring the electric charge, it the detects the energy and position on the CCD of incoming photons.

Metal Oxide Semi-conductor (MOS) CCD array

Observation from one of the two MOS CCD sensors shown in Figure 2.3. One physical pixel covers 1.1×1.1 arcsec^2, but the virtual pixels used for analysis is 50 milliarcsec. The two MOS CCDs are mounted orthogonally, so that gaps between panels on one sensor is compensated by the other. Measurements are useful in the energy range 0.3–10 keV. The MOS cameras in our data is set to full frame mode, with a time resolution of 2.6 s.

pn CCD

Observation from the pn CCD sensor shown in Figure 2.4. The pixel size is 4.1×4.1 arcsec^2 but the virtual pixels used for analysis is 50 milliarcsec. The pn camera in our data is set to extended full frame mode, with a time resolution of 199 ms. It has a lower resolution compared with the two MOS cameras but a faster readout time, which increases the time resolution and reduces the pile-up effect when several photons are counted as one with the combined energy.
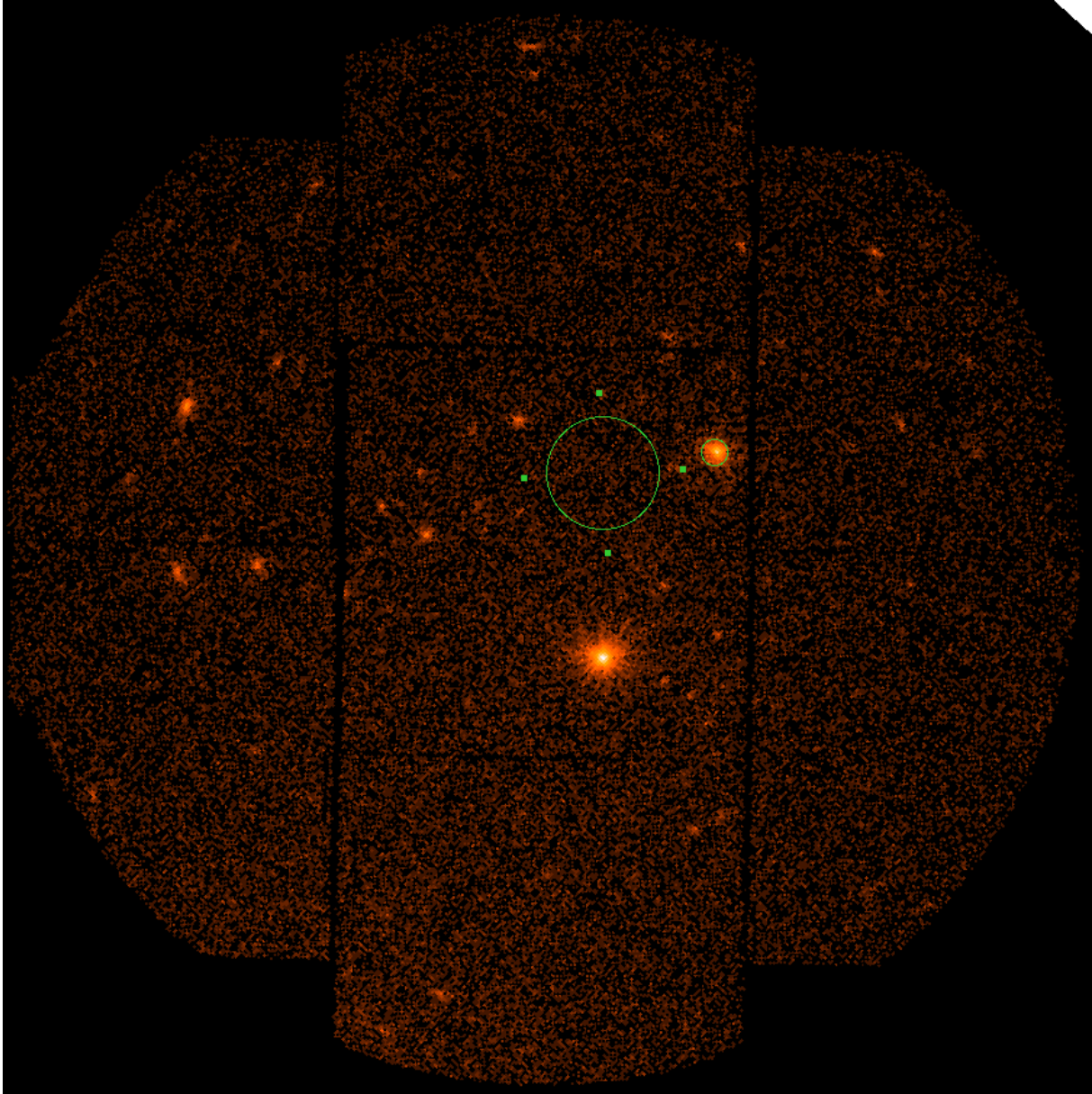
Figure 2.3: The MOS1 image of observation 0204040101 of the field including the AGN. The smaller green circle is the source region and the larger green circle is the background region. The dark lines are gaps between the individual CCD chips.
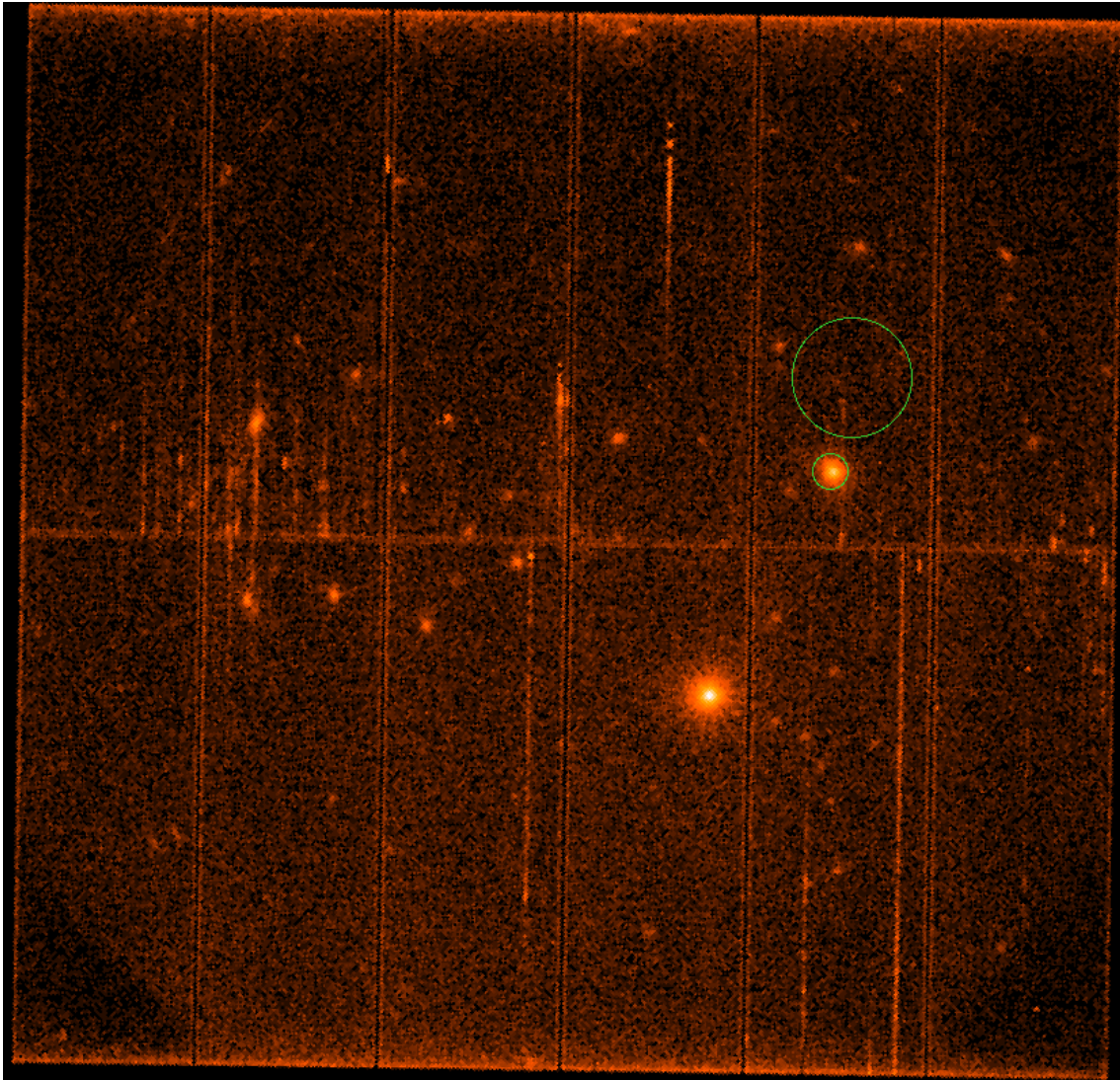
Figure 2.4: The pn image of observation 0204040101 of the field including the AGN. The smaller green circle is the source region and the larger green circle is the background region. The visible lines between the chips are filtrated away during analysis.

Chapter 3

Methods

3.1 Data reduction

Data reduction used the *XMM-Newton* Science Analysis Software v.18.0.0 tools following instructions on the *XMM-Newton* webpage[1]. Data from the three EPIC cameras were reduced individually, and the raw event lists were filtered using default values (ESA 2019). Source and background regions were manually selected by visual inspection. Using the virtual pixel size of 50 milliarcsec, for pn, the source regions varied between 428–557 pixels and the background regions between 1012–1491 pixels. For MOS, corresponding ranges are 354–493 and 1227–2209.

The source data is calibrated using a redistribution matrix file (`.rmf`) and an acilliary response file (`.arf`). The `rmf` file is a table of probabilities that a photon with the energy E will be registered with a specific energy level in the telescope. The `arf` file contains information about the effective area as a function of energy. The values in these files vary over the field of view, time and the temperature of the CCD. The background data is used as a reference in order to calibrate the source data by removing systematic background noise.

In cases of relatively high flux, several photons may be registered as the same, with a combined energy. This effect is called pile-up. In our data, we see no pile-up in the range 0.3–10 keV. Light curves for all observations were generated, with the conclusion that there was not a significant change in count rate within the observations. An example is provided in Figure 3.1.

3.2 Spectral analysis

The primary method of study used in this thesis is spectral analysis, using the data extracted as outlined in Section 3.1. This spectral analysis was done through XSPEC, an X-ray spectral

---

[1]`https://www.cosmos.esa.int/web/xmm-newton/download-and-install-sas`
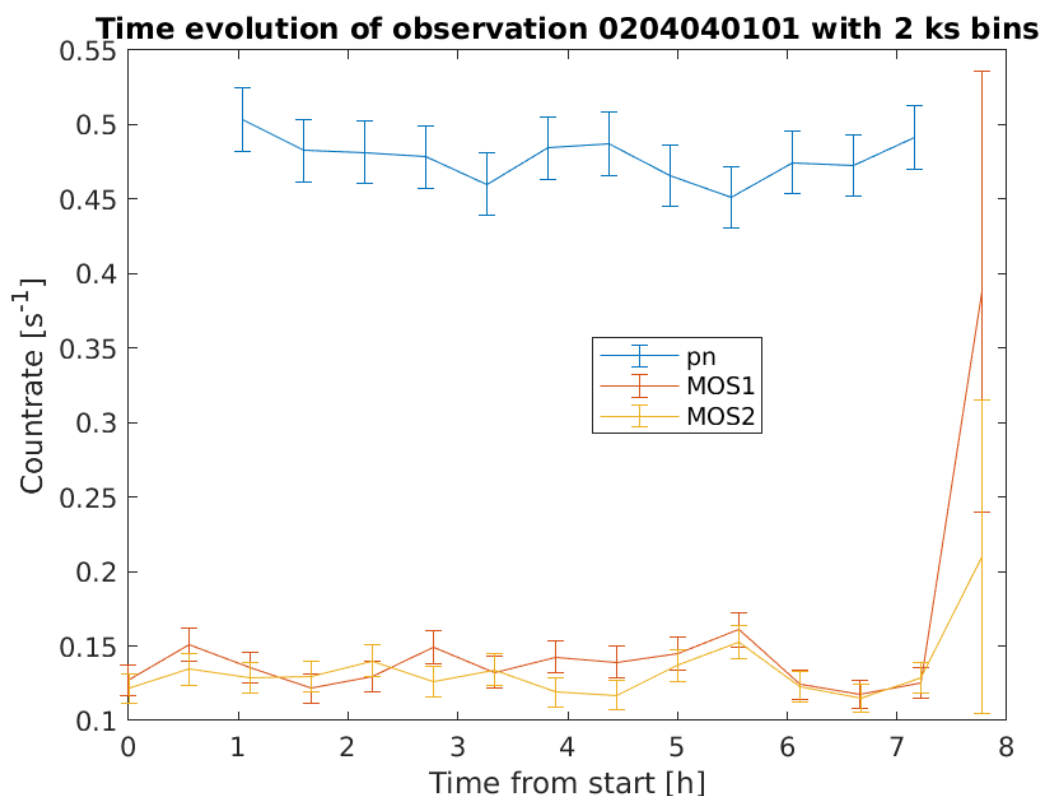
Figure 3.1: Lightcurve showing the time variation of counts per second for observation 0204040101.

fitting package (Arnaud 1996).

To analyse a spectrum in XSPEC, the data is loaded into the spectrum together with the background and response files. A model is then chosen (depending on the expected character of the source) and "folded" through the response matrix and background spectrum, so that the model and the actual data exist in the same signal space. The model is then fitted to the data with best approximations of free parameters. As such, a model's physical feasibility can be tested using the data, and hypotheses can be tested through spectral analysis. Through these tools, statistical parameters such as χ^2 values and error estimates can be obtained, giving information on the probability of different hypotheses. Also, the approximations for the parameters in the model can give information about the physical properties of the source, depending on the model used. In this thesis, a variety of models will be fit to the data.

3.2.1 XSPEC Models

The models used in XSPEC can be additive or multiplicative. Usually, the additive models correspond to different radiation sources in the studied object, while multiplicative models correspond to absorption or modification of the emitted radiation. In this thesis, the built-in XSPEC models `tbabs, zpowerlaw, zbbody, zgauss` are used. They are briefly explained below, and more information can be found at the official documentation at the XSPEC webpage[2].

Apart from these built-in models, the relativistic reflection model `relxill` is used in this thesis (Dauser, T., García, J., and Wilms, J. 2016), explained in some detail below. Full documentation can be found at the webpage of the developers.[3]

`tbabs` and `ztbabs`

`tbabs` is a multiplicative model used to model X-ray absorption in the Milky Way, with `ztbabs` being its redshifted component used for the AGN host galaxy, using the model for ISM absorption described in Section 2.4. The model has one free component: the column density of hydrogen n_H, plus the redshift z in the `ztbabs` case. The density is set to a fixed value retrieved from a table for the Milky Way component, and allowed to vary freely for the host galaxy.

`zpowerlaw`

`zpowerlaw` is an additive model of the redshifted power law, describing the hypothesised reverse Comptonized emission from the AGN corona and jet. With N_E being the number of photons cm^{-2}s^{-1}keV^{-1}, then

$$N_E = K[E(1+z)]^{-\Gamma}, \tag{3.1}$$

where K is the norm, z the redshift and Γ the photon index as described in Section 2.3.3. In this thesis, z is a known value for our particular AGN, while Γ and the norm are parameters to be determined.

`zbbody`

`zbbody` is an additive model of redshifted black-body radiation. It provides a black-body spectrum from a given peak temperature, and gives the spectrum from the Stefan-Boltzmann and Planck laws. The parameters are the maximum temperature kT (in keV), the norm and the redshift z, of which the last one is fixed while the others generally are free parameters.

---

[2]`https://heasarc.gsfc.nasa.gov/xanadu/xspec/manual/Models.html`
[3]`http://www.sternwarte.uni-erlangen.de/~dauser/research/relxill/`

zgauss

`zgauss` is an additive redshifted Gaussian distribution. It is used in this thesis to model narrow emission lines originating from the outer regions of the AGN. Its parameters are the line energy E_t, which is the peak of the Gaussian, the line width σ which corresponds to the standard deviation, and the norm. Of these, the line energy and σ are often set to specific values to look for certain line profiles, while the norm is allowed to vary.

relxill

`relxill` is a model for the relativistic reflection described in Section 2.3.6. It contains 13 different parameters, listed in Table 3.1 together with their physical interpretation. Most of these parameters will be frozen at their default values, but some important ones will be frozen at other values or (more crucially) allowed to vary.

Two of these parameters need some further explanation. Firstly, the model was found to be quite insensitive to the spin and it was therefore frozen to its maximum value of 0.998, corresponding to maximum spin in the same direction as the rotational axis, bringing the disk closer to the event horizon. Secondly, the inclination is expected to be quite low, since the AGN is radio-loud which indicates that one of the jets is pointed towards the observer. As the jets are believed to be situated perpendicular to the accretion disk, the inclination should therefore be corresponding to a "top-down" view of the accretion disk. A value of 10° was deemed to be a not too extreme value and produced quite good results.

Table 3.1: `relxill` model parameters and their values in this thesis.

Parameter	Physical interpretation	Value
a	Black hole spin	0.998
$Incl$	AGN inclination relative to the observer	$10°$
z	Redshift	0.64684
R_{in}	Inner radius of accretion disk	R_{ISCO}
R_{out}	Outer radius of accretion disk	$400R_S$
Index1 & Index2	Related to emissitivity of corona	3
R_{br}	Border between Index1 and Index2 zone	$15R_S$
E_{cut}	Observed high energy cutoff of spectrum	300 keV
Γ	Photon index of coronal power law	Free
$\log(\xi)$	$\log_{10}$ of ionisation parameter ξ	Free
R_f	Fraction of reflected and illuminating spectral components	Free
A_{Fe}	Iron abundance in disk, in units of solar abundance	Free
norm	norm of spectrum	Free

Chapter 4

Results

The main focus of this thesis is to study the properties of the supposed AGN J130028, primarily through spectral analysis. The main data source is the *XMM-Newton* telescope, but some auxilliary data is provided by the Sloan Digital Sky Survey (Aguado et al. 2019). From Sloan, we find that the object has a redshift of 0.64684, and is radio-loud.[1] The redshift places it at a distance of around 9.04 billion lightyears from Earth, according to the formula derived in Section 2.5.

For the data and results presented in this thesis, some general principles should be noted, which hold unless otherwise stated:

1. The energy levels reported are in the observed frame of reference.

2. The confidence levels are at 90% ($\Delta\chi^2 = 2.706$).

3. The error bars and confidence intervals are produced through XSPEC's `error` command.

4. For calculations of luminosity and other parameters where the calculated values may differ between *XMM*'s cameras, the value from the pn camera is always used. This is standard for handling *XMM* data, and is due to pn's larger effective area and therefore higher number of counts, providing a larger basis of data and therefore more certainty.

5. In general, the centimetre-gram-second (cgs) system of units will be used, since this is the standard in astrophysics and astronomy. Most units will be familiar to a reader used to the SI system, but the unit of energy, the *erg*, as well as power, *erg/s* are perhaps a bit more obscure. Conversions to the SI system are as follows: 1 erg $= 10^{-7}$ J, 1 erg s^{-1} $= 10^{-7}$ J s^{-1} $= 10^{-7}$ W.

---

[1]The object catalogue entry can be found at `http://skyserver.sdss.org/DR15//en/tools/explore/summary.aspx?id=1237665440442155093`

4.1   Observations

Data was acquired from the XMM database, and extracted using the XMM-SAS tools. The observations are listed in Table 4.1. Note that observation 0304320301 and 0304320201 are taken with a 25 h interval between them, so in the following analysis they are often analysed as a single observation.

Table 4.1: Observations

Obs. ID	Date [YYYY-mm-dd]	Start time [UTC]	Instrument	Counts	Exposure [ks]
0204040101	2004-06-06	19:46:20	pn	6866	21
		19:23:37	MOS1	2467	27
		19:23:37	MOS2	2437	27
0204040201	2004-06-18	17:08:27	pn	6819	21
		16:45:44	MOS1	2555	27
		16:45:44	MOS2		
0204040301	2004-07-12	16:11:20	pn	6879	21
		15:48:37	MOS1	2519	27
		15:48:37	MOS2	2483	27
0304320301	2005-06-27	05:23:04	pn	8596	23
		05:00:22	MOS1	4893	45
		05:00:22	MOS2	3998	45
0304320201	2005-06-28	21:46:20	pn	22594	58
		21:23:38	MOS1	7433	70
		21:23:38	MOS2	6222	70
0304320801	2006-06-06	23:58:39	pn	8419	27
		23:35:57	MOS1	4022	43
		23:35:57	MOS2	3662	44

4.2   Spectral analysis

The spectral analysis of J1320028 performed in this thesis was done to achieve three major goals: examining the spectral composition of the AGN to assert the radiating components

present, calculating its luminosity to get a limit on the black hole mass from the Eddington limit, and finally analysing the spectrum at different points in time to characterise the temporal evolution, if any.

This spectral analysis was done for all three cameras for each observation, tying all model parameters together except for the norms, which may differ due to errors in the camera calibrations. When multiple model components were considered, the ratio between the norms for different components was held constant. This gave some amount of freedom to compensate for the calibration, while preserving the fact that the magnitude of different model components should look the same in each camera.

The column density of hydrogen in the Milky Way for the observed coordinates was calculated using the method of Willingale et al. 2013 and was found to be 9.38×10^{19} cm^{-2}. This is in the lower end of galactic absorption, meaning that the radiation is subject to very little galactic absorption. A host galaxy absorption was also included in preliminary fits, but was found to be insignificant and is therefore not included in any further analysis.

4.2.1 Power law

First, the spectra from the six different observations of J130028 were fitted to a power-law model, which is a natural first step since most of the spectrum of AGN is expected to be described primarily by a power law. The model used in XSPEC was `zpowerlaw (zpow)`, to take into account the redshift of the source, as described in Section 3.2. The results of this fit can be seen in Table 4.2. For the three observations made in 2004, the power-law model fits remarkably well, with a reduced χ^2 very close to 1. In these three observations, no clear soft excess is present, and the power-law model is sufficient to explain the spectrum.

In the three later observations, the power-law model fit is notably worse, with the model not sufficient to explain the data. Remarkably, these do not show the usual excess at soft X-ray energies, but rather a deficit around 2 keV (observed rest frame) compared to the model, together with an excess at higher energies (> 5 keV). This is shown in Figure 4.1, which plots the three different observations from 2005–2006 with individual fits. For clarity, only the data from pn is included.

To further investigate this, data from these three later observations was fit to the power-law model in just the 2–5 keV interval in the AGN rest frame. This interval is expected from AGN theory and studies to be well explained by a simple power law, with other spectral components having a low contribution in the interval. In this interval, the fit is a bit better, but some irregularities are shown, as can be seen in Figure 4.2. This is a point of interest for further analysis of the data, but also shows that the power-law model is a good enough baseline for further analysis. Another point of interest is the varying luminosity between the three 2004 observations and the three later ones. From 2004 to 2005, the luminosity increases by a factor of around 20%, before decreasing by 10% to 2006. This points to some kind of variability of the AGN, which will be discussed further in later sections.

Table 4.2: Power law fits and parameters to the different observations

Obs. #	Obs. ID	Start date [YYYY-mm-dd]	Γ	L [10^{45} erg s^{-1}]	χ^2/dof
1	0204040101	2004-06-06	$1.85^{+0.02}_{-0.02}$	$2.08^{+0.06}_{-0.05}$	$198/192 = 1.03$
2	0204040201	2004-06-18	$1.85^{+0.03}_{-0.03}$	$2.11^{+0.06}_{-0.06}$	$130/134 = 0.97$
3	0204040301	2004-07-12	$1.85^{+0.02}_{-0.02}$	$2.12^{+0.06}_{-0.06}$	$205/196 = 1.04$
4	0304320201	2005-06-28	$1.96^{+0.01}_{-0.01}$	$2.46^{+0.04}_{-0.04}$	$429/306 = 1.40$
5	0304320301	2005-06-27	$1.94^{+0.02}_{-0.02}$	$2.44^{+0.06}_{-0.06}$	$311/246 = 1.27$
6	0304320801	2006-06-06	$1.91^{+0.02}_{-0.02}$	$2.25^{+0.06}_{-0.05}$	$289/235 = 1.23$

Table columns: (1) Observation number. (2) XMM observation ID. (3) Start date of observation. (4) power law photon index. (5) Luminosity calculated from pn camera data in the observed 0.3–10.0 keV band, in units of 10^{45} erg s^{-1}. (6) Chi-squared value divided by degrees of freedom.
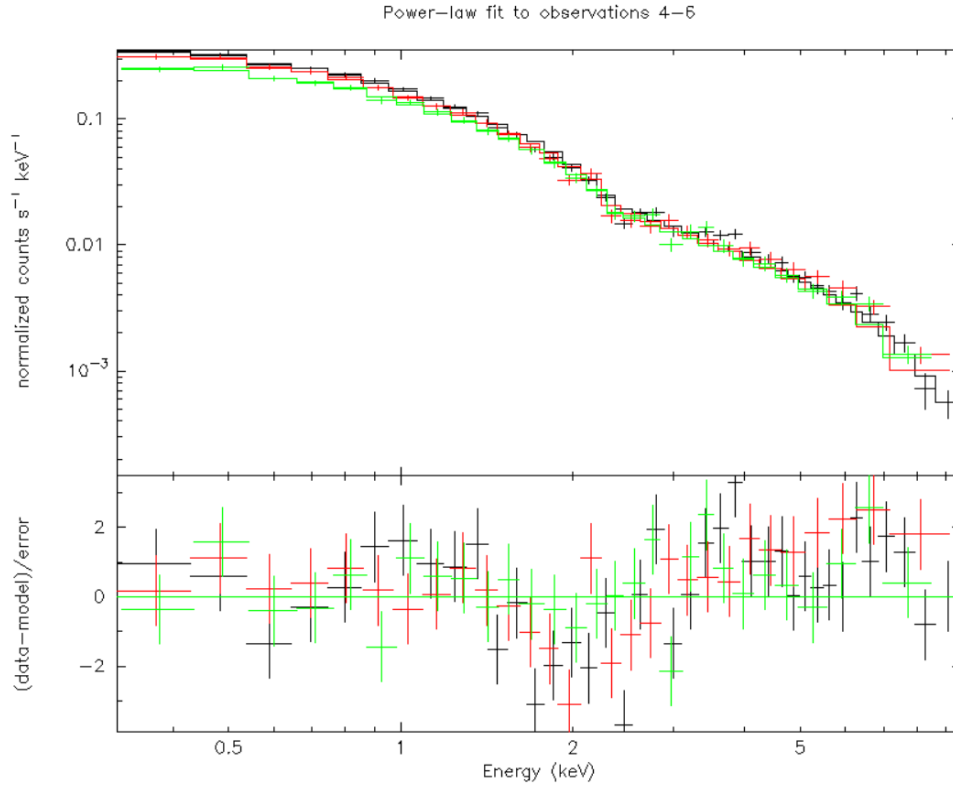
Figure 4.1: Power-law model fit to the pn data from the three 2005–2006 observations, together with the residuals in terms of sigmas. A clear deficit around 2 keV and an excess at higher energies can be seen.

4.2.2   Black-body component

For further analysis, a simple redshifted black-body component was added to the model, in the form of the `zbbody (zbb)` model in XSPEC. This is usually done to model the soft excess in AGN, to allow for more accurate determination of AGN parameters. However, as has previously been discussed in this thesis, the black-body model is not a physical representation of the soft X-ray excess, since they require too high disk temperatures. Nonetheless, it is a standard procedure and will be done here to allow comparison to similar AGN.

The black-body component was found to be insignificant in the first three observations, which is expected since the power-law model was such a good fit. For the three later observations, however, the black-body component was a notable improvement, which can be seen in Table 4.3. The spectral shape does however still show a significant soft excess, as can be
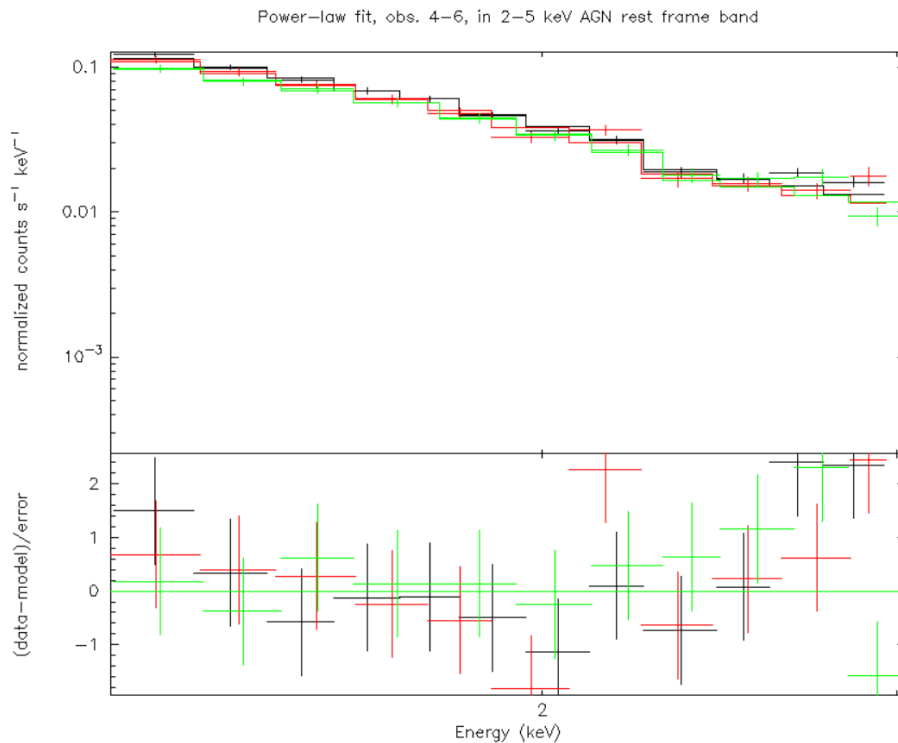
Figure 4.2: Power-law model fit to the pn camera only data from the three different 2005–2006 observations, together with the normalised residuals in terms of σ. Energy limited to the 2–5 keV band in the AGN rest frame.

seen in Figure 4.3

The higher luminosities of these three observations persist even with the black-body, as can be seen in column 5 of Table 4.3. To further examine the significance of this, the luminosity of the black-body was calculated using XSPEC's `clumin`, the results of which is presented in column 5 of Table 4.3. Peculiarly, the luminosity of the black-body component varies for the different observations, accounting for almost all of the luminosity difference for observation 5 but a smaller fraction for observations 4 and 6.
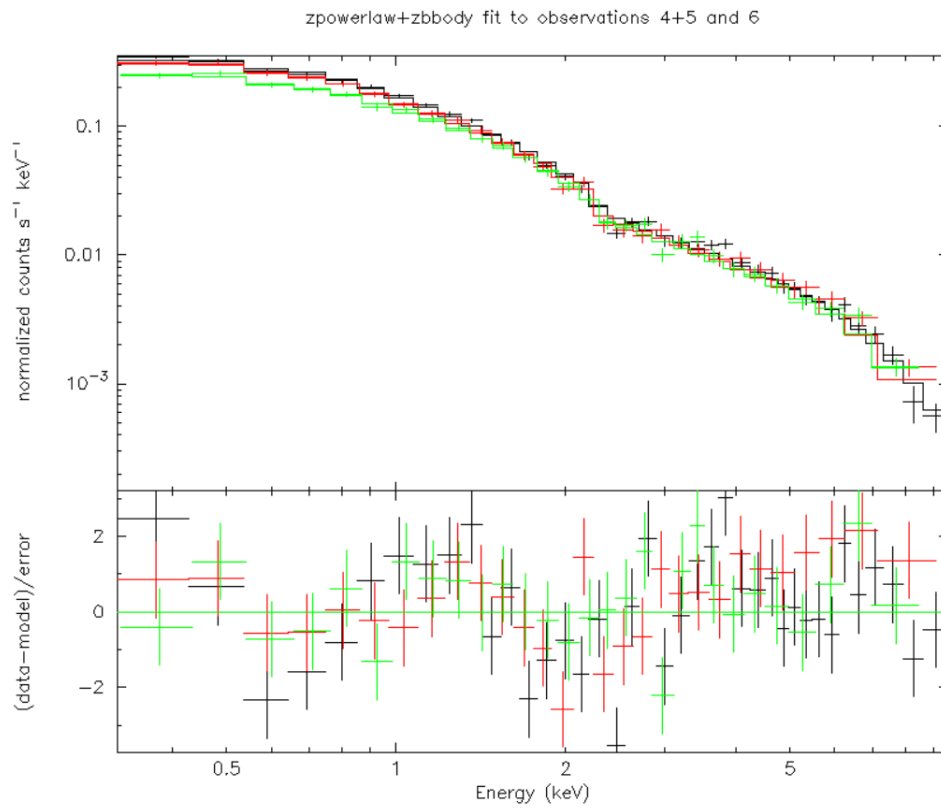
Figure 4.3: power law + black-body model fit to the pn data from the three 2005–2006 observations, together with the residuals in terms of sigmas.

Table 4.3: Black-body+power law fits and parameters to the different observations

Obs. #	Γ	kT [keV]	L [10^{45} erg s^{-1}]	L_{bbody} [10^{45} erg s^{-1}]	χ^2/dof
(1)	(2)	(3)	(4)	(5)	(6)
4	$1.86^{+0.04}_{-0.04}$	$0.25^{+0.03}_{-0.03}$	$2.49^{+0.05}_{-0.04}$	$0.15^{+0.05}_{-0.05}$	$403/302 = 1.33$
5	$1.73^{+0.06}_{-0.06}$	$0.25^{+0.01}_{-0.02}$	$2.53^{+0.07}_{-0.07}$	$0.27^{+0.06}_{-0.06}$	$261/242 = 1.08$
6	$1.83^{+0.05}_{-0.06}$	$0.27^{+0.06}_{-0.06}$	$2.29^{+0.08}_{-0.06}$	$0.074^{+0.065}_{-0.068}$	$279/231 = 1.21$

Table columns: (1) Observation number. (2) power law photon index. (3) Black-body peak temperature. (4) Luminosity calculated from pn camera data in the 0.3–10.0 keV source frame band, in units of 10^{45} erg s^{-1}. (5) Calculated luminosity in the 0.3–10.0 keV source rest-frame band of the black-body component, in the 0.3–10 keV source frame band, in units of 10^{45} erg s^{-1}. (6) Chi-squared value divided by degrees of freedom.

4.2.3 Iron line emission

In most AGN, the 6.4 keV iron K-α line is a clear feature of the spectrum, so it was initially assumed to be a part of the spectrum of J130028. The significance of the iron line in the spectrum was tested by fitting a simple `zpow+zgauss` model in the 1.5–7 keV (observed rest frame) interval, to avoid the soft excess and fit the power law to the part where it is expected to model the spectrum to the highest degree.

In Table 4.4, the significance of the iron line is shown through two different metrics: the equivalent width (EW) of the iron line, which is defined as the flux from the iron line component of the model around its peak energy, divided by the flux for the continuum emission from the other model parts at the peak energy. This is equivalent to finding the width of a rectangle (in a wavelength-flux plot) with the height equal to the continuum emission level and the same area as the integrated flux of the model component, hence the name equivalent width. This is a standard procedure performed to estimate the strength of emission and absorption line components, and can be done in XSPEC through the `eqwidth` command. As an extra measure for the iron line significance, the norm of the iron line

Table 4.4: Iron line significance

Obs. #	Iron EW [eV]	zgauss norm $[10^{-6}$ photons cm^{-2} s$^{-1}]$
(1)	(2)	(3)
1	$< 40^*$	$< 0.97^*$
2	$< 44^*$	$< 1.11^*$
3	$< 38^*$	$< 0.95^*$
4 + 5	$65.02^{+0.25}_{-0.35}$	$1.8^{+1.3}_{-1.1}$
6	$< 28^*$	$< 0.72^*$

Table columns: (1) Observation number. (2) Equivalent width of iron line component. (3) Norm of zgauss component in XSPEC.

component was also recorded. This represents the number of photons per square centimeter per second expected from the model component.

Both the norm and the EW were found to be consistent with zero for all observations except the combined 4+5 observations. To get an upper bound for the equivalent width, the norm was set to the upper limit of its 90% confidence interval and the was EW calculated for that value, producing the values found in Table 4.4.

4.2.4 Unification of spectra 4 and 5

As was mentioned earlier, observations 4 and 5 were taken with a quite short intermittent interval, with their separation time being in the order of the exposure times. Furthermore, as is clear in Figure 3.1, the variation within a single observation is quite small, justifying combining observations 4 and 5 and fitting them to the same model simultaneously. This has the benefit of combining a large amount of data, , which reduces statistical uncertainty and allows for more accurate fits and further investigations. Furthermore, from the preliminary analysis done above, observations 4 and 5 seem to have the most complex spectra, suggesting a further analysis of the state of the AGN during this time.

Therefore, all the models tested above was fit simultaneously to observations 4 and 5,

with all parameters tied between observations and cameras except for the norms, which were kept free with ratios between different model components kept constant as before. The results of this can be found in Table 4.5, and provide a baseline for further analysis, as well as investigations using more complex model.

Table 4.5: Different models fit to observations 4+5

Model	Γ	kT [keV]	Fe EW [eV]	L [10^{45} erg s^{-1}]	χ^2/dof
(1)	(2)	(3)	(4)	(5)	(6)
zpow	$1.96^{+0.01}_{-0.01}$			$2.47^{+0.03}_{-0.04}$	$745/556 = 1.34$
zpow+zbb	$1.82^{+0.03}_{-0.03}$	$0.25^{+0.02}_{-0.02}$		$2.52^{+0.04}_{-0.04}$	$678/552 = 1.23$
zpow+zgauss	$1.97^{+0.01}_{-0.01}$		$85.00^{+0.32}_{-0.17}$	$2.47^{+0.04}_{-0.03}$	$716/553 = 1.29$
zpow+zbb+zgauss	$1.84^{+0.03}_{-0.03}$	$0.25^{+0.02}_{-0.02}$	$70.64^{+0.42}_{-0.15}$	$2.51^{+0.05}_{-0.04}$	$659/549 = 1.20$

Table columns: (1) XSPEC model fit to the data. (2) Photon index. (3) Temperature of black-body component, when present. (4) Equivalent width of iron line component, when present. (5) Luminosity in observed 0.3–10 keV band. (6) Chi-squared value divided by degrees of freedom.

For this more complex spectrum, even a combined power law and black-body model together with a narrow iron line is not sufficient to explain the whole spectrum. An acceptable fit is achieved, but it is clear that the spectrum has features that has to be explained by more complex models. Moreover, as is clear from table 4.6, the luminosity of the additional components is not sufficient to explained the increased luminosity of the whole spectrum compared to observations 1–3. Therefore, we turn to `relxill`, a model for relativistic disk reflection to try to achieve a better fit. Further description of the model can be found in Section 3.2.1.

Table 4.6: Luminosity of different components of models fit to observations 4+5

| Model | L | L_Δ | L_{bbody} | L_{Fe} |
| | $[10^{45}$ erg s$^{-1}]$ | $[10^{45}$ erg s$^{-1}]$ | $[10^{45}$ erg s$^{-1}]$ | $[10^{45}$ erg s$^{-1}]$ |
(1)	(2)	(3)	(4)	(5)
zpow+zbb	$2.52^{+0.04}_{-0.04}$	$0.40^{+0.10}_{-0.10}$	$0.19^{+0.04}_{-0.04}$	
zpow+zgauss	$2.47^{+0.03}_{-0.03}$	$0.35^{+0.09}_{-0.09}$		$0.015^{+0.009}_{-0.009}$
zpow+zbb+zgauss	$2.51^{+0.05}_{-0.04}$	$0.39^{+0.11}_{-0.10}$	$0.18^{+0.04}_{-0.04}$	$0.013^{+0.009}_{-0.009}$

Table columns:(1) XSPEC model fit to the data. (2) Luminosity in observed 0.3–10 keV band. (3) Difference between luminosity of observation no. 3 and the luminosity in column 2. (4) Luminosity of black-body component. (5) Luminosity of iron-line component.

4.2.5   `relxill`

To get a first look at the `relxill` model, it was fit together with a `tbabs` and a `zgauss` model to the combined observations 4+5, the result of which can be found in Table 4.7. For the parameters not included in the table, a few things should be noted. The inclination of the black hole was set to 10°, to model the jets being pointed in the direction of the Earth, since the AGN is radio-loud. Furthermore, the fit proved to be quite insensitive to the spin of the black hole, which was set by the fit to its maximum value of 0.998 but with inconsistent error bars. Therefore, the spin was frozen at this value to allow for better fitting of the other parameters. This insensitivity of the model to the spin parameter is likely tied to the low iron abundance of the best fits, which was consistent with 0. These results will be discussed further in Section 5.2. For the parameters present in Table 4.7, the $\log(\xi)$ parameter was consistent with 0, although this was somewhat dependent on the particular fit. The other parameters took on more expected values, with a softer photon index than the power law of observations 1–3 and with a reflection fraction indicating the presence of reflected radiation.

To further improve the fit, an additional black-body component was added, which seemed to be significant enough to justify its inclusion in the best-fit model. For this model, the iron abundance and ionisation parameter was also consistent with 0, but the ionisation parameter covered a larger range. Nonetheless, this model is the best fit yet to the complex spectrum

of observations 4+5, but some physical properties of the spectrum seem to not be explained in the model. This will be discussed in Chapter 5. The data and error plots (pn camera only) can be found in Figure 4.4, with the corresponding model found in Figure 4.6. For comparison, the same observations without the additional black-body component can be found in Figure 4.5. For this `relxill` model, a partial covering of the AGN by absorbing material was also tried (XSPEC method `pcf`) but was found to be insignificant.

Table 4.7: Comparison of low-iron `relxill` fits to combined observations 4+5

Model	Γ	$\log(\xi)$	R_f	kT	L	χ^2/dof
				[keV]	[10^{45} erg s^{-1}]	
(1)	(2)	(3)	(4)	(5)	(6)	(7)
relxill + zgauss	$2.04^{+0.02}_{-0.02}$	< 0.20	$0.54^{+0.15}_{-0.12}$	-	$2.61^{+0.04}_{-0.05}$	$639/546 = 1.17$
relxill + zgauss + zbbody	$2.04^{+0.04}_{-0.07}$	$0.31^{+0.56}_{-0.31}$	$0.80^{+0.19}_{-0.32}$	$0.38^{+0.08}_{-0.04}$	$2.63^{+0.12}_{-0.08}$	$612/542 = 1.13$

Table columns: (1) XSPEC model. (2) power law photon index. (3) $\log_{10}$ of ionisation parameter ξ. (4) Fraction of reflected and illuminating spectral components. (5) Black-body peak temperature in keV. (6) Luminosity in observed 0.3–10 keV band. (7) χ^2 value divided by degrees of freedom.

As a final investigation, the `relxill` model was fit to all observations, to try the best-fit model for all observations. A black-body component was added for observation 6 but found to be insignificant for the first three observations, as before. The results of this can be found in Table 4.8. As can be seen in the table, the reflection fraction was quite low for observations 1–3. Since the `relxill` model approaches a simple power-law model as the fraction of reflected radiation approaches 0, this means that the fit to observations 1–3 is quite similar to ones found in Table 4.2.
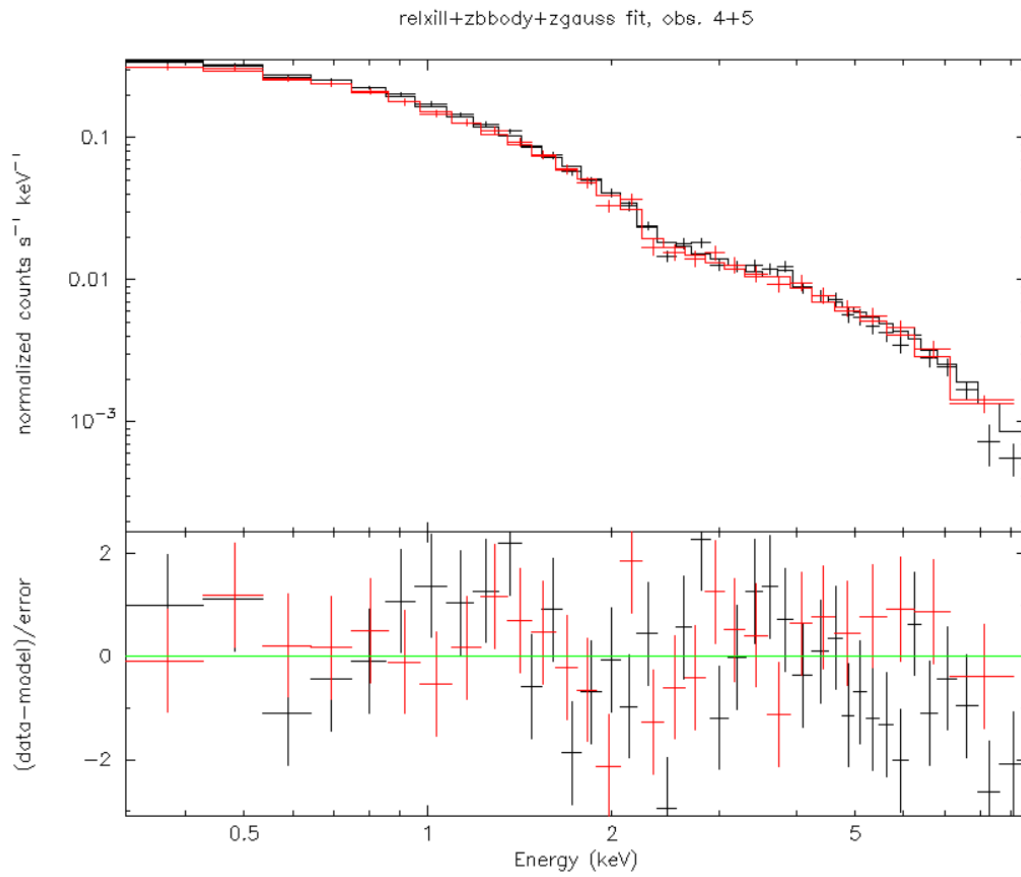
Figure 4.4: relxill, black-body and iron line model fit to the pn data from observations 4+5. Notable is the bump around 1 keV and the deficit at 2 keV.
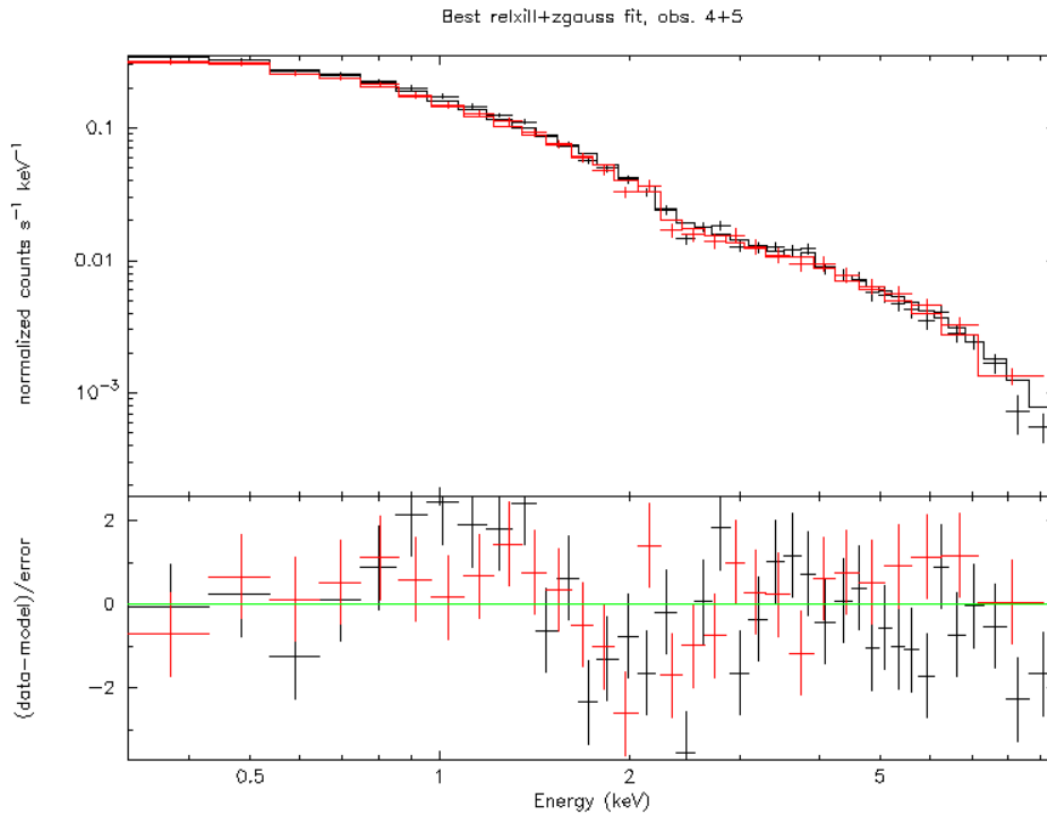
Figure 4.5: relxill and iron line model without additional black-body component fit to pn data from observations 4+5. Note the larger error bars and increased excess at 1 keV compared to Figure 4.4.
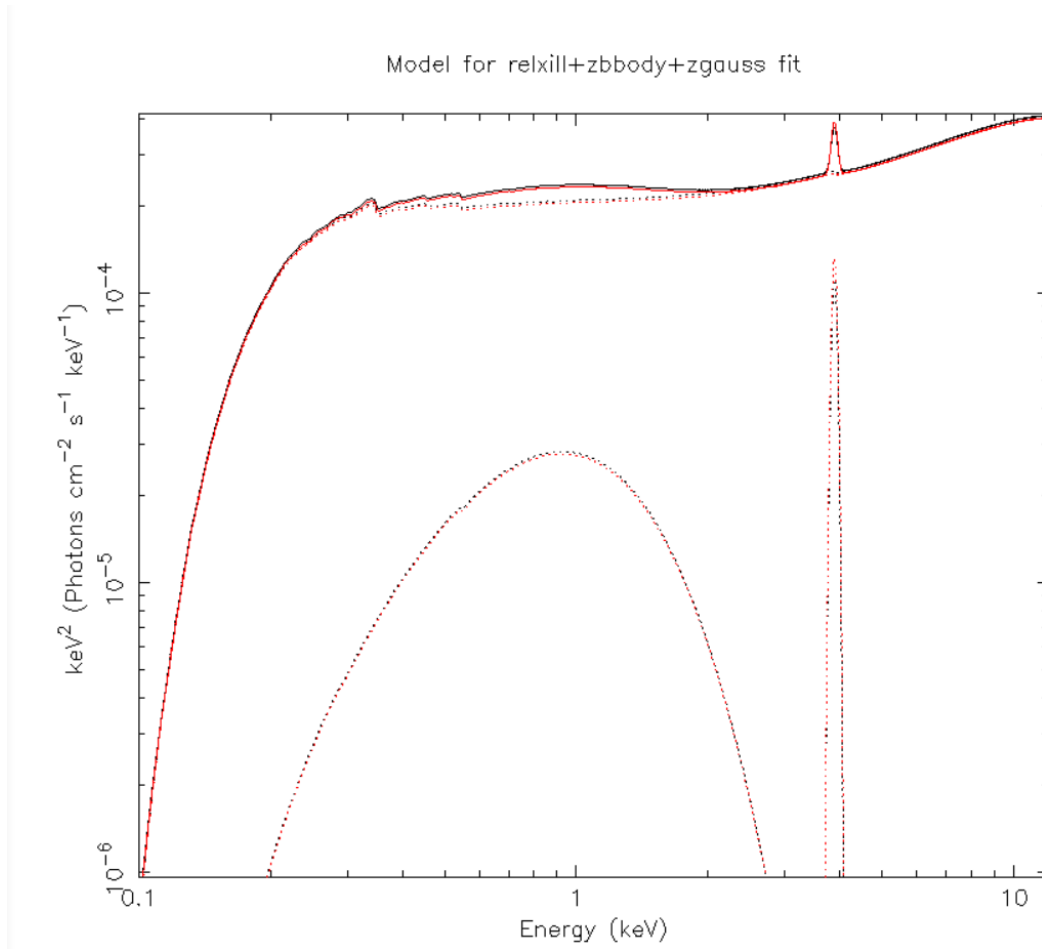
Figure 4.6: relxill, black-body and iron line model for the fit in Figure 4.4. Note the peak of the black-body component at 1 keV and the clearly visible iron line.

Table 4.8: Best `relxill` (and additional models where applicable) fits

Observation	Γ	$\log(\xi)$	R_f	$\dfrac{A_{\mathrm{Fe}}}{A_{\mathrm{Fe},\odot}}$	L [10^{45} erg s^{-1}]	χ^2/dof
(1)	(2)	(3)	(4)	(5)	(6)	(7)
1	$1.84^{+0.10}_{-0.03}$	$2.3^{+1.6}_{-2.3}$	$0.16^{+0.29}_{-0.13}$	4.66^*	$2.11^{+0.14}_{-0.14}$	$196/189 = 1.04$
2	$1.84^{+0.14}_{-0.03}$	$2.3^{+1.0}_{-2.3}$	$0.27^{+0.35}_{-0.20}$	4.96^*	$2.16^{+0.71}_{-0.08}$	$125/131 = 0.95$
3	$1.84^{+0.09}_{-0.03}$	$2.3^{+0.3}_{-2.3}$	$0.17^{+0.15}_{-0.17}$	4.80^*	$2.16^{+0.15}_{-0.13}$	$202/193 = 1.05$
4+5	$2.04^{+0.04}_{-0.07}$	$0.3^{+0.6}_{-0.3}$	$0.80^{+0.19}_{-0.32}$	$\approx 0^*$	$2.63^{+0.12}_{-0.08}$	$612/542 = 1.13$
6	$2.08^{+0.14}_{-0.11}$	$\approx 0^*$	$1.37^{+1.24}_{-0.69}$	$\approx 0^*$	$2.40^{+0.06}_{-0.04}$	$260/230 = 1.13$

Notes: For observations 4+5 and 6, an additional `zbbody` component was added for the best fit. In 4+5, a `zgauss` component is also present. Values marked with * gave inconsistent results in XSPEC, giving no consistent error ranges. **Table columns:** (1) Observation number. (2) power law photon index. (3) $\log_{10}$ of ionisation parameter ξ (4) Fraction of reflected and illuminating spectral components. (5) Iron abundance in accretion disk, in units of solar abundance. (6) Luminosity in observed 0.3–10 keV band. (7) Chi-squared value divided by degrees of freedom.

4.3   Mass and Eddington ratio estimation

As described in Section 2.2.2, the Eddington luminosity is proportional to the mass of an AGN. For our object, we can use Equation 2.6 in two different ways. Either to get a lower limit on the mass of the AGN by assuming the maximum observed luminosity to be the Eddington luminosity, or by using other mass estimates to estimate the Eddington ratio.

4.3.1   Estimation of mass

To get a lower limit on the black hole mass in the AGN, some assumptions need to be made. First of all, we assume that the black hole is at its Eddington limit, as stated above. Secondly, we need to account for the fact that the luminosity calculated in this report is only in a limited energy band, most commonly in the (observed) 0.3–10 keV band. For the calculations used in Equation 2.6, the total, or *bolometric*, luminosity is needed, and here the methods used in Netzer 2019 will be employed. The bolometric luminosity is calculated by using a bolometric correction factor: $L_{\text{bol}} = k_{\text{bol}} L_{\text{obs}}$. This k_{bol} is different for different parts of the spectra, and here a factor for the 2–10 keV band will be used according to

$$k_{\text{bol}} = 7 \cdot (L_{\text{obs}}/10^{42} \text{ erg s}^{-1})^{0.3}. \tag{4.1}$$

It should be noted that this factor introduces a lot of uncertainty to the calculations, since the bolometric correction factor makes some large assumptions about the shape of the spectrum. This uncertainty is likely of a much larger magnitude than the statistical errors in the luminosity calculated from the spectrum, but the error range produced will not be discussed in this thesis. Nevertheless, it provides the best method available to get an estimation of the Eddington ratio and mass. To get the best estimation for the mass limit, the best-fit `relxill` model for observations 4+5 was used, and the resulting correction factor, bolometric luminosity and mass lower bound can be found in the first row of Table 4.9.

4.3.2   Eddington ratio

To get an estimation of the Eddington ratio of the AGN, another method of estimating the black hole mass is needed. We found an estimation of the black hole mass in a catalog of AGN black hole masses captured in the Sloan Digital Sky Survey (Shen et al. 2008). The catalog gave a black hole mass of $10^{9.804} M_\odot$, and again using Equation 2.6 the Eddington luminosity could be calculated and from that the Eddington ratio according to $R_{\text{Edd}} = L_{\text{obs}}/L_{\text{Edd}}$. This was done for observations 1, 4+5 and 6, to get a measure of how the Eddington ratio changes over time. Observations 2 and 3 were emitted due to being very close in time to observation 1, with their spectra also being very similar, making observation 1 quite sufficient to study

Table 4.9: Mass and Eddington ratio estimations

Obs.	Model	L_{obs}	L_{bol}	R_{Edd}	M_{BH}
		$[10^{45}\ \mathrm{erg\ s^{-1}}]$	$[10^{45}\ \mathrm{erg\ s^{-1}}]$		$[10^8\ \mathrm{M_\odot}]$
(1)	(2)	(3)	(4)	(5)	(6)
4+5	`relxill`	$1.19^{+0.02}_{-0.05}$	$70.0^{+1.6}_{-3.7}$	$1^\dagger$	$> 5.56^{+0.13}_{-0.30}$
1	`zpow`	$1.04^{+0.01}_{-0.02}$	$58.2^{+1.0}_{-1.1}$	$0.0726^{+0.0012}_{-0.0014}$	$63.68^\ddagger$
4+5	`relxill`	$1.19^{+0.022}_{-0.05}$	$69.9^{+1.6}_{-3.7}$	$0.0874^{+0.0020}_{-0.0046}$	$63.68^\ddagger$
6	`relxill`	$1.09^{+0.01}_{-0.08}$	$62.3^{+0.45}_{-5.5}$	$0.0779^{+0.0006}_{-0.0069}$	$63.68^\ddagger$

Table columns: (1) Observation number. (2) XSPEC model used. (3) Calculated luminosity in the 2–10 keV AGN source frame band. (4) Bolometric luminosity calculated with bolometric correction factor. Error ranges are statistical errors from XSPEC, the errors from bolometric correction are not included. (5) Estimated Eddington ratio. (6) Estimated mass. †: Eddington ratio is assumed to be 1 to get a lower bound on the AGN mass. ‡: Mass taken from Sloan Digital Sky Survey.

the temporal evolution. The results of this calculation can be found in the lower three rows of Table 4.9.

Chapter 5

Discussion

The AGN studied in this thesis shows some interesting properties seen in the results above. These will be discussed in this section, followed by a summary of the findings of the thesis in the final chapter.

5.1 Spectral evolution over time

First of all, the first three observations are quite well described by a simple power-law model, as outlined in Section 4.2.1. This power-law radiation likely has its origin in the jet of the AGN, since the jet is present in the radio-band. The X-ray spectrum being described by a power law is somewhat atypical for AGN, which usually require other components to explain parts of the spectrum, particularly the soft excess. As noted in Section 2.3.5, the soft excess is almost ubiqutous in AGN, but here it seems to be absent.

For observations 4, 5 and 6, the power-law model is a notably worse fit than for the other observations. In Figure 4.1, it is clear that the poorer quality of the fit is due to the soft excess as well as some discrepancies with the model at the higher end of the spectrum. These discrepancies are further characterised by the 2–5 keV AGN rest frame fit shown in Figure 4.2, which shows that the spectrum expected to be modelled well by the power law is much more consistent than the other parts. As is clear in Table 4.3 and Figure 4.3, the addition of the black-body component does not fully remedy these discrepancies, as the fits are still notably worse than the other ones. Furthermore, the change in luminosity is not fully covered by the addition of the black-body component, as shown in Table 4.6. However, the addition of the black-body does make the photon index more similar to the values for the earlier observations, and the temperature of the black-body component is right in the middle of the distribution of soft excess temperatures, as shown by Gierliński and Done 2004. This might point to a usual soft excess being present, but together with a different spectral component that is harder to model.

A further change between the different spectra is the presence of the narrow iron line in observations 4+5 and its seeming absence not only in observations 1–3 but also in observation 6. This shows that the spectral shape of the AGN did not only change in the presence of the soft excess after 2004, but also has an iron line. It is clearly visible in 2005 but has disappeared in 2006, which indicates that either the geometry of the AGN or the emission regions themselves have changed. The low width of the line points to its source being far from the black hole, as described in Section 2.3.2. Still, it is possible that even narrow-line features are variable on a timescale of a year, so the result is not unreasonable but rather interesting.

Then, there is also the 20% increase in luminosity corresponding with the change in spectral shape between observations 1–3 and 4+5, coupled with a 10% decrease for observation 6. This change is correlated with and might be caused by the change in spectral shape, but further study would be needed to investigate and justify this conclusion.

5.2   relxill – our best effort at describing the spectrum

The best hypothesis for the changing spectrum presented in this thesis is the disk reflection model `relxill`. As is clear in Table 4.7 and Figure 4.4, this presents a better model for the soft excess and high-energy discrepancies than any other tried in this thesis. It is however not perfect, and as can be seen in Figure 4.6, it notably requires an extra black-body component to explain a part of the soft excess located around 1 keV, which theoretically should be included self-consistently in the disk reflection model. This black-body component has an unusually high temperature for the regular soft excess black-body, and probably points to some physical phenomenon which is not easily explained by the disk reflection model.

Furthermore, the parameters in the `relxill` model are quite hard to constrain due to the relatively poor quality of the fit. This makes it hard to make comparisons with other AGN analysed with similar models, and points in the same direction of unexplained physics as previously discussed. Still, something could be said about the iron abundance of the disk, which was found to be consistent with 0 for observations 4–6, as presented in Table 4.8. This is unusual, since most AGN are found to have iron abundances around solar levels, as reported by Walton et al. 2013 and Crummy et al. 2006. This means that if the model is valid, then the low iron abundance is unusual for AGN. This low iron abundance also makes an accurate measurement of the black hole spin hard, since the spin is closely related to the smearing of the iron K-α line, and is usually measured this way. This means that the low iron abundance probably explains the insensitivity to the spin parameter in our `relxill` fits, as mentioned in Section 4.2.5. It should also be noted that the usual supersolar iron abundance of AGN is also a matter of some contention in the field. (García et al. 2018). In light of this, the result of low iron abundance in J130028 could be due to the `relxill` model expecting a higher iron abundance, which itself might not be physically accurate. Therefore,

a further study of J130028 and its iron abundance could be an interesting proposition. Lastly the very low value of the $\log(\xi)$ parameter in `relxill` is also somewhat hard to analyse, due to the large error bars and it being consistent with 0 in most fits. However, this low value also points to something unusual with the fit, since it is outside the range reported by other sources (Walton et al. 2013; Crummy et al. 2006).

Still, the presence of some disk reflection in this AGN is a tentative conclusion one could draw, together with some kind of change or covering of this feature in some observations. This is most probably due to the geometry of the AGN, but to discern its nature would require further study. A primary goal of further studies would be to find a better-fitting model for the spectrum, to be able to more efficiently constrain the AGN parameters.

Chapter 6

Summary and Conclusions

The goal of this thesis was to investigate a hitherto unstudied active galactic nucleus and try to discern its emission processes, estimate its mass and examine its evolution over time. In short, the findings could be described as follows: This seems to be an AGN with a high black hole mass and Eddington ratio of around 10%, which is quite typical. Despite this, the AGN changes its spectrum quite dramatically over a period of one year, going from a simple power-law spectrum to a possible disk reflection spectrum. This change in the spectral shape is correlated by an increase in the luminosity of the AGN, suggesting some kind of obscuration or other geometrical variation in the AGN regions. The disk reflection model does not fully model the spectrum, suggesting physics at play which are not captured by the model.

To further study this AGN, the reflection model used for the later observation could be further tweaked or changed. The `relxill` model package presents different geometries for the radiation illuminating the disk, as well as other options that are beyond the scope of this thesis. Apart from this, more observations to analyse could shine a light on the further temporal evolution of this AGN. Currently, only observations from *ROSAT* in 1991 exist, but this particular AGN might be captured again by *XMM* or by other telescopes. The physics of AGN test the absolute limits of our scientific understanding of the universe, and many mechanisms of AGN emission and development are as of yet poorly understood. The empirical data is notably hard to explain fully by any theoretical models, and there remains many observed AGN which have yet to be studied. Future analysis of this data together with even better X-ray telescopes and expanded theoretical models will probably deepen our understanding of these objects which push the limits of the laws of physics, and thereby our understanding of the universe we live in and its evolution.

Bibliography

Lynden-Bell, D. (Aug. 1969). "Galactic Nuclei as Collapsed Old Quasars". In: *Nature* 223.5207, pp. 690–694. DOI: 10.1038/223690a0.

Shakura, N I and Rashid Alievich Sunyaev (1973). "Black holes in binary systems. Observational appearance." In: *Astronomy and Astrophysics* 24, pp. 337–355.

Willis, A. G., R. G. Strom, and A. S. Wilson (Aug. 1974). "3C236, DA240; the largest radio sources known". In: *Nature* 250.5468, pp. 625–630. DOI: 10.1038/250625a0.

Kellermann, K. I. et al. (Oct. 1989). "VLA Observations of Objects in the Palomar Bright Quasar Survey". In: 98, p. 1195. DOI: 10.1086/115207.

Arnaud, K. A. (1996). "XSPEC: The First Ten Years". In: *Astronomical Data Analysis Software and Systems V*. Ed. by George H. Jacoby and Jeannette Barnes. Vol. 101. Astronomical Society of the Pacific Conference Series, p. 17.

Fabian, A.C. et al. (2000). "Broad iron lines in active galactic nuclei". In: *Publications of the Astronomical Society of the Pacific* 112.775, p. 1145.

Wilms, J, A Allen, and R McCray (2000). "On the absorption of X-rays in the interstellar medium". In: *The Astrophysical Journal* 542.2, p. 914.

Davis, Tamara M and Charles H Lineweaver (2001). "Superluminal recession velocities". In: *AIP Conference Proceedings*. Vol. 555. 1. American Institute of Physics, pp. 348–351.

Strüder, L. et al. (2001). "The European Photon Imaging Camera on XMM-Newton: The pn-CCD camera". In: *A&A* 365.1, pp. L18–L26. DOI: 10.1051/0004-6361:20000066. URL: https://doi.org/10.1051/0004-6361:20000066.

Turner, M. J. L. et al. (2001). "The European Photon Imaging Camera on XMM-Newton: The MOS cameras". In: *A&A* 365.1, pp. L27–L35. DOI: 10.1051/0004-6361:20000087. URL: https://doi.org/10.1051/0004-6361:20000087.

Gierliński, Marek and Chris Done (Mar. 2004). "Is the soft excess in active galactic nuclei real?" In: *Monthly Notices of the Royal Astronomical Society* 349.1, pp. L7–L11. ISSN: 0035-8711. DOI: 10.1111/j.1365-2966.2004.07687.x. eprint: https://academic.oup.com/mnras/article-pdf/349/1/L7/11183290/349-1-L7.pdf. URL: https://doi.org/10.1111/j.1365-2966.2004.07687.x.

Crummy, Jamie et al. (2006). "An explanation for the soft X-ray excess in active galactic nuclei". In: *Monthly Notices of the Royal Astronomical Society* 365.4, pp. 1067–1081.

Bonning, Erin W et al. (2007). "Accretion disk temperatures and continuum colors in QSOs". In: *The Astrophysical Journal* 659.1, p. 211.

Middelberg, Enno and Uwe Bach (May 2008). "High resolution radio astronomy using very long baseline interferometry". In: *Reports on Progress in MiddelbPhysics* 71.6, p. 066901. DOI: 10.1088/0034-4885/71/6/066901. URL: https://doi.org/10.1088%2F0034-4885%2F71%2F6%2F066901.

Shen, Yue et al. (June 2008). "Biases in Virial Black Hole Masses: An SDSS Perspective". In: *The Astrophysical Journal* 680.1, pp. 169–190. DOI: 10.1086/587475. arXiv: 0709.3098 [astro-ph].

Beckmann, Volker (2012). *Active Galactic Nuclei.* eng. 1st ed.. ISBN: 9783527666812.

Fabian, A.C. (2012). "Observational Evidence of Active Galactic Nuclei Feedback". In: *Annual Review of Astronomy and Astrophysics* 50.1, pp. 455–489. DOI: 10.1146/annurev-astro-081811-125521. eprint: https://doi.org/10.1146/annurev-astro-081811-125521. URL: https://doi.org/10.1146/annurev-astro-081811-125521.

Hwang, Ho Seong et al. (2012). "Activity in galactic nuclei of cluster and field galaxies in the local universe". In: *Astronomy & Astrophysics* 538, A15.

Netzer, Hagai (2013). "Nonthermal radiation processes". In: *The Physics and Evolution of Active Galactic Nuclei.* Cambridge University Press, pp. 23–34. DOI: 10.1017/CBO9781139109291.003.

Walton, DJ et al. (2013). "Suzaku observations of bare active galactic nuclei". In: *Monthly Notices of the Royal Astronomical Society* 428.4, pp. 2901–2920.

Willingale, R. et al. (May 2013). "Calibration of X-ray absorption in our Galaxy". In: *Monthly Notices of the Royal Astronomical Society* 431.1, pp. 394–404. DOI: 10.1093/mnras/stt175. arXiv: 1303.0843 [astro-ph.HE].

Dauser, T., García, J., and Wilms, J. (2016). "Relativistic reflection: Review and recent developments in modeling". In: *Astronomische Nachrichten* 337.4-5, pp. 362–367. DOI: 10.1002/asna.201612314. eprint: https://onlinelibrary.wiley.com/doi/pdf/10.1002/asna.201612314. URL: https://onlinelibrary.wiley.com/doi/abs/10.1002/asna.201612314.

García, JA et al. (2018). "The problem of the high iron abundance in accretion disks around black holes". In: *arXiv preprint arXiv:1805.00581.*

Aguado, David Sánchez et al. (2019). "The fifteenth data release of the Sloan Digital Sky Surveys: first release of MaNGA-derived quantities, data visualization tools, and stellar library". In: *The Astrophysical Journal Supplement Series* 240.2, p. 23.

ESA (June 2019). *How to filter EPIC event lists for flaring particle background.* https://www.cosmos.esa.int/web/xmm-newton/sas-thread-epic-filterbackground. (Accessed on 03/18/2020).

Netzer, Hagai (2019). "Bolometric correction factors for active galactic nuclei". In: *Monthly Notices of the Royal Astronomical Society* 488.4, pp. 5185–5191.

Reynolds, Christopher S (2019). "Observing black holes spin". In: *Nature Astronomy* 3.1, pp. 41–47.